Reconstructing the spatial distribution of the relative shear modulus in quasi-static ultrasound elastography: plane stress analysis

L. Seppecher, Elie Bretin, Pierre Millien, Lorena Petrusca, Elisabeth Brusseau

Reconstructing the spatial distribution of the relative shear modulus in quasi-static ultrasound elastography: plane stress analysis

Laurent Seppecher[a], Elie Bretin[b], Pierre Millien[c], Lorena Petrusca[d], Elisabeth Brusseau[d,*]

[a]*Institut Camille Jordan, Ecole Centrale de Lyon & UCBL, Lyon, France*
[b]*Institut Camille Jordan, INSA de Lyon & UCBL, Lyon, France*
[c]*Institut Langevin, CNRS UMR 7587, ESPCI Paris, PSL Research University, Paris, France*
[d]*Univ Lyon, INSA-Lyon, Université Claude Bernard Lyon 1, UJM Saint-Etienne, CNRS, Inserm, CREATIS UMR 5220, U1294, Lyon, France*

---

*Corresponding Author: Elisabeth Brusseau, Bâtiment Léonard de Vinci - 21 avenue Jean Capelle, 69621 Villeurbanne, France; Email, elisabeth.brusseau@creatis.insa-lyon.fr; Phone, +33 4 72 43 61 41

Article published in Ultrasound in Medicine and Biology, 49(3):710-722, 2023.

Abstract

Quasi-static ultrasound elastography (QSUE) is an imaging technique that mainly provides axial strain maps of tissues, when the latter are subjected to compression. In this article, a method for reconstructing the relative shear modulus distribution within a linear elastic and isotropic medium, in QSUE, is introduced. More specifically, the plane stress inverse problem is considered. The proposed method is based on the variational formulation of the equilibrium equations and on the choice of adapted discretization spaces, and only requires displacement fields in the analyzed media to be determined. Results from plane stress and 3D numerical simulations, as well as from phantom experiments, showed that the method is able to reconstruct the different regions within a medium, with shear modulus contrasts that unambiguously reveal whether inclusions are stiffer or softer than the surrounding material. More specifically, for the plane stress simulations, inclusion-to-background modulus ratios were found to be very accurately estimated, with an error lower than 3%. For the 3D simulations, for which the plane stress conditions are no longer satisfied, these ratios were, as expected, less accurate with an error that remained lower than 10% for two of the three cases analyzed, but which was around 34% for the last case. Concerning the phantom experiments, a comparison with a shear wave elastography technique from a clinical ultrasound scanner was also made. Overall, the inclusion-to-background shear modulus ratios obtained with our approach were found to be closer to those given by the phantom manufacturer, than the ratios provided by the clinical system.

Keywords: Ultrasound imaging, Quasi-static ultrasound elastography, Inverse problem, Shear modulus contrast

---

Introduction

Many diseases are known to be associated with changes in the mechanical properties of tissues (Krouskop et al. (1998); Mazza et al. (2007)). Accessing local values of elasticity- or viscoelasticity-related parameters can therefore provide useful information for diagnosis, and has led to the development of elastography techniques (Ophir et al. (1991)). Various elastographic approaches have been described in the literature, all sharing the same underlying principle: imaging and analyzing the tissue response to a mechanical perturbation, to extract a parameter of interest. Depending on the imaging modality employed (e.g., ultrasound imaging, magnetic resonance imaging), the type of mechanical stress used (e.g., compression, harmonic excitation), and the parameter to be determined (e.g., axial strain, shear modulus), different techniques have been introduced. For a more detailed overview of the variety of developments achieved in elastography, we refer the reader to the following references (Bamber et al. (2013); Mariappan et al. (2010); Parker et al. (2011); Wang and Larin (2015)).

This article focuses more particularly on quasi-static ultrasound elastography (QSUE), where the deformation of tissues subjected to some compression is analyzed (Varghese (2009)). Although the information produced is generally limited to strain images, QSUE has proven to be a valuable technique for distinguishing regions that differ in stiffness within a medium, and its evaluation as a diagnostic tool has been the subject of many studies (Cosgrove et al. (2013); Gong et al. (2011); Itoh et al. (2006); Lyshchik et al. (2005)). In particular, different work comparing strain and shear wave elastography

reported similar diagnostic performances for the two techniques (Chang et al. (2013); Kim et al. (2018); Seo et al. (2018); Youk et al. (2014)). A major application of QSUE is the differentiation between benign and cancer tissues, which has led to the investigation of specific criteria. As an example, the strain ratio between a suspicious area and a reference region represents a straightforward indicator to compare these two tissues (Lyshchik et al. (2005); Cho et al. (2010); Waage et al. (2011)). Such a ratio, but computed this time from the elastic modulus estimates, has also been reported to be helpful in distinguishing benign from malignant lesions in shear wave elastography (Berg et al. (2012); Au et al. (2014)). In QSUE, however, the strain ratio only partially reflects the contrast in the elastic modulus between the selected regions, as the stress distribution is not uniform within the scanned area.

Generally speaking, the inverse problem of determining the elastic modulus or the stiffness contrast within a medium has been widely studied (Doyley (2012); Ammari et al. (2015); Widlak and Scherzer (2015); Barbone and Oberai (2007)). The main difference between solving this problem in dynamic and quasi-static elastography is that the acceleration term is null in the second case. Among the methods used in QSUE is the direct inversion, as proposed by Nitta and Shiina to recover the spatial distribution of the Young's modulus E in a 3D body (Nitta and Shiina (2000)). The method consists of substituting, in the equilibrium equations, the stress terms using the material constitutive law. Assuming that the Poisson's ratio is known and constant throughout the medium, this results in equations in which the

unknowns are the spatial derivatives of E, divided by E. With this method, modulus values (in kPa) can be accessed, provided that additional information (e.g., the surface Young's modulus) is known. In a previous study, Sumi et al. (1995) similarly investigated the reconstruction of the shear modulus μ for a linear elastic and isotropic material through 1D and 2D approaches. As no initial information on modulus values is available *a priori* for biological tissues, the authors suggested positioning some material with known mechanical properties on the surface of the region to be examined, so as to provide a reference for the method. Because of its simplicity, direct inversion is an attractive method. Nevertheless, it requires differentiating the displacement but also the strain fields, which will negatively impact the results if the displacements are initially affected by noise.

Iterative methods have also been developed for the estimation of the material constitutive law parameters. They are based on the formulation of the inverse problem as an optimization problem in which the modulus values are iteratively varied until minimizing an error between the displacements or strains determined by solving the forward problem and those measured experimentally (Doyley et al. (2000); Baldewsing et al. (2005, 2006)). Solving the forward problem requires knowledge of the boundary conditions, which makes this method difficult to use for clinical applications. Moreover, the computational cost associated with this approach can be heavy, as a solution of the forward problem needs to be computed at each iteration.

Recently, preliminary results have been reported using machine learning (Hoerig et al. (2017, 2019)). This field, which can be applied in countless areas, is also employed in numerous applications in medical imaging. In Ho-

erig et al. (2017, 2019), a neural network-based approach is used to learn the stress-strain relationship of the material, and the mechanical parameters of choice are then deduced from the estimated stresses and strains. However, this technique also involves finite element modeling of the experiment and requires a set of force-displacement measurements as input data.

The present study focuses on the shear modulus contrast reconstruction of linear elastic and isotropic media in quasi-static ultrasound elastography. Recently, mathematical developments for analyzing the inverse elasticity problem were performed, and some results presented (Ammari et al. (2021); Brusseau et al. (2021)). In this paper, the plane stress inverse problem is more particularly investigated. The proposed method is based on the variational formulation of the equilibrium equations and on the use of a suitable finite element discretization technique, and requires only the displacement fields within the examined media to be determined beforehand.

This article is organized as follows. In the next section, the relative shear modulus reconstruction method is described in detail, as well as the media used for the method assessment and the ultrasound data acquisition. Results obtained from numerical simulations and phantom experiments are then presented and discussed. In particular, a comparison is made with a shear wave elastography technique from a clinical ultrasound scanner for the experimental data. Concluding remarks are provided in the last section.

Methods

This study focuses on the reconstruction of shear modulus maps up to a multiplicative constant, in linear elastic and isotropic media, from displacement fields obtained in quasi-static ultrasound elastography. A main difficulty associated with this inverse problem is that, under compression, biological tissues undergo 3D deformation, whereas the data generally available in ultrasound imaging are 2D images, giving access to in-plane motion only. To overcome this problem, we assume that the plane stress conditions are satisfied, conditions that have already been chosen in various other elastography studies, such as in Seidl et al. (2019) and in Karimi et al. (2013). It should be emphasized that neither plane stress nor plane strain makes it possible to exactly describe the medium deformation when it is compressed with the ultrasound transducer. However, the choice of plane stress versus plane strain was made here, as the displacement fields measured experimentally were found to be closer to those obtained in the plane stress case, when modeling the corresponding experiments using a finite element method-based simulation software (COMSOL Multiphysics, COMSOL AB, Stockholm, Sweden, www.comsol.com). The method developed is fully described below.

Relative shear modulus map reconstruction

Let us consider a linear elastic and isotropic medium. The constitutive equation of such a medium is:

$$\sigma_{ij} = 2\mu\varepsilon_{ij} + \lambda\delta_{ij}\varepsilon_{kk} \tag{1}$$

with λ and μ the Lamé parameters, σ_{ij} and ε_{ij} the components of the stress and strain tensors, σ and $\mathcal{E}$, respectively, δ_{ij} the Kronecker delta, and ε_{kk},

the trace of $\mathcal{E}$. We assume that a displacement field $\boldsymbol{u}$ or a sequence of displacement fields $\boldsymbol{u}_1, \ldots, \boldsymbol{u}_n$, is measured inside this medium. We also assume that these fields result from a quasi-static elastography experiment and that they all satisfy the same system of equilibrium equations. Neglecting the body forces, these equations write

$$\nabla \cdot \sigma = \mathbf{0}, \tag{2}$$

and combining (1) and (2) gives

$$\nabla \cdot \big(2\mu \mathcal{E}(\boldsymbol{u})\big) + \nabla(\lambda \nabla \cdot \boldsymbol{u}) = \mathbf{0}, \tag{3}$$

with $\mathcal{E}(\boldsymbol{u}) := \big(\nabla \boldsymbol{u} + (\nabla \boldsymbol{u})^\top\big)/2$, the strain tensor, and $\nabla\cdot$ and ∇, the divergence and gradient operators, respectively. Note that if $\boldsymbol{u}$ is known, then (3) is a linear and homogeneous system of three equations with respect to the unknown pair (λ, μ). As a homogeneous system, (3) can be solved only up to a global multiplicative constant, additional scalar information being necessary for the Lamé parameters to be determined.

Under the plane stress conditions, the three stress tensor components σ_{xz}, σ_{yz}, and σ_{zz} are equal to 0. Consequently, (3) is reduced to two equations and the two strain tensor components, ε_{xz} and ε_{yz}, are null as well. Moreover, $\sigma_{zz} = 0$ gives:

$$2\mu\varepsilon_{zz} + \lambda(\varepsilon_{xx} + \varepsilon_{yy} + \varepsilon_{zz}) = 0, \tag{4}$$

i.e.,

$$\varepsilon_{zz} = -\frac{\lambda}{2\mu + \lambda}(\varepsilon_{xx} + \varepsilon_{yy}), \tag{5}$$

and

$$\nabla \cdot \boldsymbol{u} = \frac{2\mu}{2\mu + \lambda}(\varepsilon_{xx} + \varepsilon_{yy}), \tag{6}$$

which leads to

$$\lambda \nabla \cdot \boldsymbol{u} = \frac{2\mu\lambda}{2\mu + \lambda}(\varepsilon_{xx} + \varepsilon_{yy}). \tag{7}$$

At this step, we can note that estimating displacements in the imaging plane ($\boldsymbol{u}_{2D}$) will provide all the information needed for the inverse problem to be solved. Furthermore, this method is intended for the examination of biological tissues, which are characterized by values of λ much higher than those of the shear modulus. With $\lambda \gg \mu$, (3) and (7) lead to

$$\nabla \cdot \big(\mu \mathcal{E}(\boldsymbol{u}_{2D})\big) + \nabla(\mu \nabla \cdot \boldsymbol{u}_{2D}) \approx \mathbf{0}, \tag{8}$$

and reconstructing the spatial distribution of the relative shear modulus will finally be performed by considering the following homogeneous system of two equations

$$\nabla \cdot \big(\mu \mathcal{E}(\boldsymbol{u}_{2D})\big) + \nabla(\mu \nabla \cdot \boldsymbol{u}_{2D}) = \mathbf{0}, \tag{9}$$

with $\mu(x, y)$, the only unknown and $\boldsymbol{u}_{2D}(x, y)$, the 2D displacement estimated from ultrasound images. For simplification purposes, $\boldsymbol{u}_{2D}$ will be denoted $\boldsymbol{u}$ in the remainder of the article.

General principle

Let us consider a 2D domain Ω, which can be any region of interest in the 2D image, within which the displacement field $\boldsymbol{u}$ has been estimated. As the unknown elastic parameter μ can be discontinuous, we look for it as an element of the parameter space $M := L^2(\Omega)$. Moreover, a variational

approach is used here, which consists of choosing a Hilbert space of test functions, to give a weak formulation of the equilibrium equations (9). As no boundary information is available, we propose to use a class of functions that vanish at this boundary. We therefore introduce $V := H_0^1(\Omega, \mathbb{R}^2)$ that is a classic Sobolev space defined as

$$V := \left\{ \boldsymbol{v} \in L^2\big(\Omega, \mathbb{R}^2\big) |\ \nabla \boldsymbol{v} \in L^2\big(\Omega, \mathbb{R}^{2\times 2}\big),\ \boldsymbol{v}|_{\partial\Omega} = \mathbf{0} \right\}. \tag{10}$$

Multiplying (9) by $\boldsymbol{v} \in V$ and integrating by parts lead to

$$\int_\Omega \mu(\mathcal{E}(\boldsymbol{u}) : \mathcal{E}(\boldsymbol{v}) + (\nabla \cdot \boldsymbol{u})(\nabla \cdot \boldsymbol{v})) = 0 \quad \forall \boldsymbol{v} \in V, \tag{11}$$

with $\mathcal{E}(\boldsymbol{u}) : \mathcal{E}(\boldsymbol{v}) := \sum_{ij} \mathcal{E}(\boldsymbol{u})_{ij} \mathcal{E}(\boldsymbol{v})_{ij}$.

To build a finite dimensional system of equations, we approach the two function spaces M and V by finite dimensional discretization subspaces $M_h \subset M$ and $V_h \subset V$, where $h > 0$ is a parameter of discretization. Denoting $\big(e_1^{M_h}, \dots e_{\dim M_h}^{M_h}\big)$ a basis of M_h, and $\big(\boldsymbol{e}_1^{V_h}, \dots \boldsymbol{e}_{\dim V_h}^{V_h}\big)$ a basis of V_h, we decompose any function $m \in M_h$ as

$$m = \sum_j m_j e_j^{M_h}, \tag{12}$$

and from (11), we deduce the following finite dimensional system of equations

$$\sum_j \mu_j \int_\Omega e_j^{M_h} (\mathcal{E}(\boldsymbol{u}) : \mathcal{E}(\boldsymbol{e}_i^{V_h}) + (\nabla \cdot \boldsymbol{u})(\nabla \cdot \boldsymbol{e}_i^{V_h})) = 0 \quad \forall i \in \{1, \dots, \dim V_h\}. \tag{13}$$

This is a homogeneous linear system of $\dim V_h$ equations involving $\dim M_h$ unknowns. Denoting the real vector $\boldsymbol{\mu} := (\mu_1, \ldots, \mu_{\dim M_h})^\top$, this system is written in a matrix form as

$$\mathcal{A}\boldsymbol{\mu} = \mathbf{0}, \tag{14}$$

where $\mathcal{A}$ is a large sparse matrix, given by

$$\mathcal{A}_{ij} := \int_\Omega e_j^{M_h}(\mathcal{E}(\boldsymbol{u}) : \mathcal{E}(\boldsymbol{e}_i^{V_h}) + (\nabla \cdot \boldsymbol{u})(\nabla \cdot \boldsymbol{e}_i^{V_h})). \tag{15}$$

The problem is now reduced to finding non-zero solutions of (14), which is equivalent to finding the null space of the matrix $\mathcal{A}$. As this problem may not have non-zero solutions, the determination of the relative shear modulus spatial distribution can be reformulated as a minimization problem, such as

$$\begin{aligned} &\underset{\boldsymbol{\mu}}{\text{minimize}} \, \|\mathcal{A}\boldsymbol{\mu}\|_2^2 \\ &\text{s.t. } \mu_k = 1, \forall k \in K \end{aligned} \tag{16}$$

with, here, the constraint that the value of μ_k is equal to 1, $\forall k \in K$, with K the set of indices corresponding to any region running along the image borders, and assumed to be part of the background. In practice, with our data, a region of interest will be selected within which the reconstruction will be performed. All indices outside this region will belong to K.

Determining the null space of the matrix $\mathcal{A}$ is equivalent to determining the null space of $\mathcal{A}^\top\mathcal{A}$, which is a symmetric square matrix of smaller size than $\mathcal{A}$ as soon as the system is overdetermined. Thus, in this work, the

problem solved is finally

$$\begin{aligned} &\underset{\boldsymbol{\mu}}{\text{minimize}} \left\| \mathcal{A}^\top \mathcal{A} \boldsymbol{\mu} \right\|_2^2 \\ &\text{s.t. } \mu_k = 1, \forall k \in K. \end{aligned} \tag{17}$$

Use of multiple data

For multiple data, that is, when a sequence of displacement fields $\boldsymbol{u}_1, \ldots, \boldsymbol{u}_n$ is available, it is very easy to take these different fields into account. For each displacement field $\boldsymbol{u}_\ell$, we build the corresponding sparse system defining the matrix $\mathcal{A}_\ell$, as described above (15). The multiple data problem is then formulated as

$$\begin{aligned} &\underset{\boldsymbol{\mu}}{\text{minimize}} \left\| \mathbb{A}^\top \mathbb{A} \boldsymbol{\mu} \right\|_2^2 \\ &\text{s.t. } \mu_k = 1, \forall k \in K \end{aligned} \qquad \text{with } \mathbb{A} := \begin{pmatrix} \mathcal{A}_1 \\ \vdots \\ \mathcal{A}_n \end{pmatrix}. \tag{18}$$

Honeycomb space discretization

The choice of a pair of discretization spaces M_h and V_h is crucial, and is certainly a key question for this inversion. We found that a very efficient discretization technique with excellent numerical stability is the honeycomb space discretization.

The domain $\Omega \subset \mathbb{R}^2$ is covered by a hexagonal honeycomb tiling of edge size $h > 0$, as illustrated in Figure 1. Thus, Ω is decomposed as

$$\overline{\Omega} = \bigcup_{k=1}^{N_h} \overline{\Omega_k^h}, \tag{19}$$

where Ω_k^h are the open hexagons. We choose the parameter approximation space M_h as the class $\mathbb{P}^0\left(\{\Omega_k^h\}\right)$ of functions that are constant in each hexagon. More precisely,

$$M_h := \left\{ \mu \in L^2(\Omega) |\ \mu|_{\Omega_k} \text{ is constant for each } k \right\}. \tag{20}$$

A canonical basis of M_h is simply given by $e_k^{M_h} := \mathbf{1}_{\Omega_k}$ for $k = 1, \ldots, N_h$.

We now choose a corresponding test function subspace $V_h \subset V$ that connects the hexagons together. To do so, sub-discretization $\{\tau_k^h\}$ of Ω is performed using an adapted equilateral triangulation (Fig. 1). We define V_h as a subset of the classic $\mathbb{P}^1\left(\{\tau_k^h\}, \mathbb{R}^2\right)$ finite element class. More precisely, for each intersection node p_i of three adjacent hexagons, φ_i is defined as the unique function of $H^1(\Omega)$ that is linear in each triangle, and satisfies $\varphi_i(p_i) = 1$ and cancels at any other nodes of the triangular sub-mesh (Fig. 2). We then define the vector-valued test functions

$$\boldsymbol{e}_{ik}^{V_h}(x, y) := \varphi_i(x, y) \begin{bmatrix} \delta_{1k} \\ \\ \delta_{2k} \end{bmatrix} \quad k = 1, 2, \tag{21}$$

for i such that p_i is an intersection node of three hexagons. The space V_h is the subspace of V generated by these functions.

$$V_h := \operatorname{span}\left\{ \boldsymbol{e}_{ik}^{V_h} |\ i \in I,\ k \in \{1, 2\} \right\}, \tag{22}$$

where I is the set of indices of all intersection nodes of three adjacent hexagons.

Finally, the method described constructs an approximation of the relative shear modulus in M_h, as a piecewise constant function on the honeycomb discretization. In order to obtain a smoother result, we project the reconstruction on $\mathbb{P}^1\left(\{\tau_k^h\}\right)$, the class of continuous piecewise linear functions on

the triangulation. It should be noted that for all of the results presented later in this article, the edge size h of the honeycomb tiling was set at 0.7 mm. This value was found to be adapted to the sampling of the data used.

Solution computation

Different efficient methods can be used to solve (17) or (18), and in this work, we used *CVX* (Grant and Boyd, 2014, 2008). For the results shown below, the computation time required for this step was only a few seconds on a standard laptop.

Displacement field estimation and regularization

The reconstruction method uses displacement fields as input data. The initial displacement fields are estimated using our method previously developed for strain imaging (Brusseau et al., 2014). The basic principle of this method is briefly recalled here. Additional information can be found in the cited paper.

Let us consider two radiofrequency ultrasound images, I_1 and I_2, that are acquired before and after, or during, medium compression. The first image is partitioned into many regions of interest (2D ROIs), regularly spaced and of equal size, and for each one of these ROIs, its deformed replica is searched for in I_2. To describe the ROI transformation between images, 2D translation and axial scaling are considered. For each ROI, these parameters are determined via the maximization of the correlation coefficient between the pre- and post-deformation regions. It should be noted that, with this approach,

the axial strain ε can be directly deduced from the axial scaling factor α ($\varepsilon = \alpha - 1$), without requiring any derivative computation.

During experiments, rather than only two images, a sequence of radiofrequency frames is generally acquired, which can be used to estimate the required fields. In that case, medium-compression related parameters are computed for pairs of successive images, and the resulting information is combined to provide the final displacement maps.

An example of displacement field $\boldsymbol{u}$ obtained with this method is shown in Figure 3, resulting from a phantom experiment (CIRS model 049, Type III inclusion, corresponding to case #8 later in the article). The axial and lateral components are denoted u_y and u_x, respectively. We can clearly see a difference in quality between these two components, which is typical of ultrasound elastography measurements. The axial displacement appears to be very smooth and usable, whereas the lateral displacement needs to be regularized before being used. For a more in-depth analysis of this difference, it is also relevant to provide the images of the derivatives of $\boldsymbol{u}$ (Fig. 4), which are, furthermore, necessary for the construction of the matrix $\mathcal{A}$. We note that the inclusion is easy to locate in the fields corresponding to the derivatives of u_y, contrary to the derivatives of the lateral displacement field u_x, which are dominated by noise.

To improve the lateral displacement, both the axial and lateral components are used, while keeping in mind that the field that really needs to be modified is the lateral component. More precisely, the approach consists of minimizing

the following energy $J := J_{\text{reg}} + J_{\text{data},\boldsymbol{u}}$, where

$$J_{\text{reg}}(\boldsymbol{w}) := \int_\Omega 2\mu^*(\|\mathcal{E}(\boldsymbol{w})\|^2 + (\nabla \cdot \boldsymbol{w})^2), \tag{23}$$

is an elastic regularization term, and

$$J_{\text{data},\boldsymbol{u}}(\boldsymbol{w}) := \frac{1}{r_x}\int_\Omega (u_x - w_x)^2 + \frac{1}{r_y}\int_\Omega (u_y - w_y)^2, \tag{24}$$

represents the discrepancy functional.

In this work, μ^* is set at 1 and the parameters r_x and r_y associated with each component of $\boldsymbol{u}$ are adjusted accordingly. In particular, to preserve the axial field while allowing more important variations in the lateral field, the value of r_y should be much lower than r_x. From a numerical point of view, the minimum $\boldsymbol{w}$ of J is computed via finite element discretization, and only requires the resolution of a linear system. An example of results obtained with the fields shown in Figures 3 and 4 is given in Figure 5, using $1/r_x = 15 \cdot 10^{-2}$, and $1/r_y = 15$. We observe that w_x is a smooth version of u_x, and now smooth enough to make the inclusion easily detectable on its derivatives.

Simulation and phantom description, ultrasound data acquisition

The method for mapping the relative stiffness within a medium was applied to simulated and experimental data.

Numerical simulations were performed using Comsol Multiphysics. Two kinds of situations were analyzed, considering the plane-stress (cases #1-3)

and 3D (cases #4-6) problems. For the 3D problem, three parallelepiped-shaped media were built, measuring 60 mm x 40 mm x 40 mm (length x width x height) and which all consist of a 10-mm-diameter spherical inclusion embedded in the middle of a homogeneous background, the different regions being made of a linear elastic and isotropic material. In one case (case #4), the inclusion is softer than the background, with a shear modulus of 4 kPa vs. 9 kPa for the surrounding material, whereas in the two other cases, the inclusions are stiffer, with shear moduli of 16 kPa (case #5, modulus ratio = 16/9) and 27 kPa (case #6, modulus ratio = 27/9). For all regions, the Lamé parameter λ was adjusted to obtain a Poisson's ratio of 0.495, a value typically used for the simulation of media in elastography studies (Nayak et al. (2017); Poul and Parker (2021); Thittai et al. (2012)). To get closer to the experimental conditions, the configuration of compression of the medium with the ultrasound probe was reproduced, resulting in only part of the medium top surface being subjected to displacement (Fig. 6). The probe was positioned above the inclusion and displaced vertically, downward. To determine whether the results could be influenced by the level of compression applied, three displacement values were considered, 0.4 mm, 0.8 mm and 1.2 mm, corresponding to 1%, 2% and 3% axial strain, respectively. The bottom surface was fixed, whereas the vertical ones were free to move. In this work, relative shear modulus maps are reconstructed from the 2D displacements estimated in the ultrasound imaging plane. With the simulations performed, the axial and lateral displacements retained were those of the vertical plane crossing the center of the spherical inclusion, as illustrated in Figure 6. Finally, the same media, but this time considering

the plane stress problem, were also simulated (cases #1-3). In all cases, no noise was added to the data. When reconstructing the relative shear modulus maps, the estimated inclusion-to-background shear modulus ratios are therefore expected to be close to 0.44 (cases #1 and #4), 1.78 (cases #2 and #5), and to 3 (cases #3 and #6), whatever the applied compression.

Experimental tests were carried out with two CIRS phantoms (Computerized Imaging Reference Systems, Norfolk, VA, USA), the models 049 and 059. The CIRS model 049 (Elasticity QA) consists of a parallelepiped-shaped medium, within which several spherical inclusions are embedded. The inclusion position, size, and Young's modulus as well as the modulus of the background material are specifications provided by the manufacturer. For this phantom, two different regions were scanned, both containing a 10-mm-diameter spherical inclusion. In the first region, the inclusion of Young's modulus of 13 kPa (Type II inclusion) is softer than the surrounding medium with a modulus of 26.5 kPa (case #7), whereas in the other case, the 47-kPa inclusion (Type III inclusion) is stiffer than the background (case #8). The second CIRS phantom (model 059 or breast elastography phantom) is characterized by an overall shape that mimics the breast of a patient in the supine position. This phantom contains several spherical inclusions that are stiffer than the surrounding material. The Young's moduli of the inclusions and the background are 43.3 kPa and 13 kPa, respectively. Two different areas were also scanned, one showing the presence of a single inclusion (case #9), the other, two inclusions one below the other (case #10). For each region examined, a typical quasi-static elastography experiment was performed, i.e.,

the operator cautiously compressed the medium with the hand-held probe while radiofrequency images were acquired. Data were collected using an Ultrasonix ultrasound scanner (Ultrasonix Medical Corporation, Richmond, BC, Canada), equipped with an L14-5W/60 linear array transducer. The sampling frequency was 40 MHz. For these phantom data, the inclusion-to-background shear modulus ratios estimated from the reconstructed maps, are expected to be close to 0.49 (cases #7), 1.77 (cases #8), and to 3.33 (cases #9 and #10).

Analysis of the results and comparison with a shear wave elastography technique

For all the media described above, the relative shear modulus maps were reconstructed and the inclusion-to-background stiffness ratios computed. These ratios were obtained by selecting circular regions (ROIs) of the same size inside the inclusion and the background (excluding the transition zone), and by computing the ratio of their mean values. For each case, two ratios were determined, R_1 and R_2, from two different regions in the background. As is done in clinical practice, the ROI selection was performed manually, which inevitably has an impact on the results. For that reason, a third ratio was reported, R_{tb}, considering this time the total background. As the media analyzed in this study consist of inclusions embedded in homogeneous background materials, R_{tb} appears particularly adapted for the method assessment.

To complete the analysis of the experimental results, a comparison with a shear wave elastography technique was also made, using an Aixplorer ul-

trasound scanner (SuperSonic Imagine, Aix-en-Provence, France) equipped with an SL15-4 linear array transducer (Bercoff et al. (2004)). This clinical system provides images of the Young's modulus of tissues computed as three times the shear modulus (3μ), considering that the media investigated are linear elastic, isotropic, and (quasi-) incompressible (Tanter et al. (2008)). Any Young's modulus ratio is therefore equal to the shear modulus ratio, which allows a direct comparison with the results from our technique. The selection of circular ROIs was here also performed manually using the tools available on this ultrasound system. These tools do not allow to extract information concerning the whole background, which prevents the ratio R_{tb} from being determined.

Results and Discussion

Results from the numerical simulations and experiments with phantoms are detailed below. Relative shear modulus images are shown for all the cases described in the previous section. It should be specified that, as the reconstructed maps are obtained up to a multiplicative constant, we chose to divide them by their minimum value before display. These maps are, therefore, without unit.

Simulation results

For each case, three relative shear modulus maps were reconstructed from the three different data sets corresponding to distinct levels of compression. To quantify the variations between the reconstructed maps, the absolute difference was computed. In all cases, this difference remains locally lower than 10^{-8}, which explains that no visual differences between the three maps

can be observed and that the inclusion-to-background modulus ratios do not vary. For those reasons, in the following, results will be presented without making any distinction regarding the applied compression.

The reconstructed maps obtained with the plane stress and 3D simulations are displayed in Figures 7 and 8, respectively. In all cases analyzed, the inclusions are easily detectable in the images, and they appear stiffer or softer than the background in agreement with the mechanical properties chosen for the different media. However, some differences can be observed between Figures 7 and 8. The shape of the inclusions, first, is well preserved with the plane stress simulations (Fig. 7), whereas in Figure 8, a weak deformation of these inclusions (with a clearer illustration in Fig. 8a) can be noted. Then, the different regions appear relatively homogeneous in the plane stress results whereas more variations are visible for the 3D simulations. To provide a more quantitative assessment of the results, inclusion-to-background shear modulus ratios are reported here (Table 1). For the plane stress simulations, these ratios are $R_1 = 0.43$, $R_2 = 0.43$ and $R_{tb} = 0.44$ for case #1, $R_1 = 1.81$, $R_2 = 1.81$ and $R_{tb} = 1.81$ for case #2, and $R_1 = 3.11$, $R_2 = 3.11$ and $R_{tb} = 3.08$ for case #3, and are in perfect agreement with the mechanical description of the chosen numerical models. The relative error expressed as a percentage, also called the percentage error and computed as $100 \times |1 – R_{tb}/R_{theo}|$ with R_{theo} the theoretical ratio, was determined and found to be lower than 3% in the three cases examined. For the 3D simulations, the ratios are $R_1 = 0.55$, $R_2 = 0.58$ and $R_{tb} = 0.60$ for case #4, $R_1 = 1.60$, $R_2 = 1.69$ and $R_{tb} = 1.68$ for case #5, and $R_1 = 2.62$, $R_2 = 2.79$ and $R_{tb} = 2.74$ for case #6. The different values of ratios for

each case illustrate the stronger variations in the background observed in the reconstructed maps. However, the difference in the values remains limited. Moreover, compared with the plane stress simulation results, these ones show a higher deviation from the theoretical values, which remains lower than 10% for cases #5 and #6, but reaches around 34% for case #4. Such a higher deviation could be expected, as in this work, a plane-stress-based approach was developed for reconstructing maps of the relative shear modulus within media. When plane stress conditions are no longer satisfied, as with the 3D simulations, errors in the determined ratios occur. However, the proposed method allows us to clearly identify the different regions within a medium, and despite a reduction in the elastic contrast observed in cases #4-6, this method should remain useful for elastography purposes.

Experimental results

Relative shear modulus maps obtained with the experimental data are presented in Figure 9. As with the simulation results, the inclusions can be easily identified in the elastograms and two inclusions, even spatially close, can remain clearly distinguishable, as can be seen in Figure 9d. For each case, inclusion-to-background modulus ratios are also provided here (Table 2), with an illustration of ROI selection in Figure 11. For the model 049, the following ratios were obtained, $R_1 = 0.50$, $R_2 = 0.52$ and $R_{tb} = 0.52$ for case #7, and $R_1 = 1.73$, $R_2 = 1.77$ and $R_{tb} = 1.76$ for case #8. These values are very close to those expected, 0.49 and 1.77, respectively. For the breast phantom (model 059), however, the ratios were found to be lower than the target value, 3.33. Indeed, for the area containing a single inclusion (case #9), $R_1 = 2.51$, $R_2 = 2.69$ and $R_{tb} = 2.60$, and for the two inclusion case

(#10), these ratios were: $R_1 = 2.48$, $R_2 = 2.70$ and $R_{tb} = 2.35$ for the top inclusion, and $R_1 = 2.46$, $R_2 = 2.68$ and $R_{tb} = 2.49$ for the bottom one. For a more complete analysis of the results, a comparison with a shear wave elastography technique, the one available in the Aixplorer ultrasound scanner, was conducted. Elastograms obtained with this technique are presented in Figure 10, along with an illustration of ROI selection for modulus ratio computation in Figure 11. For the CIRS model 049, the modulus ratios here were found to be 0.49 and 0.50 for case #7 and 1.38 and 1.59 for case #8. For the breast phantom, these values were 2.11 and 2.19 for the region containing a single inclusion (case #9), and for the other region 2.01 and 2.33 for the top inclusion and 2.30 and 2.34 for the bottom one (case #10). It is interesting to note that except for case #7, the ratios provided by this technique are further from the expected values than those obtained with our method.

The relative shear modulus maps presented in this article are the very first ones reconstructed with the proposed method. The latter is able to clearly reveal regions differing in stiffness within a medium, and the results were found not to be affected by a variation in the level of compression applied. For all media analyzed, inclusions appeared stiffer or softer than the background in agreement with the mechanical properties chosen for the numerical models or the Young's modulus values provided by the manufacturer for the phantoms. Moreover, the inclusion-to-background modulus ratios obtained with the plane stress simulations were very close to the actual values. For the model 049 also, these ratios were in perfect agreement with the target

values, whereas for the 3D simulations and experimental results with the breast phantom, some differences were observed between estimated and expected ratios. In this work, to overcome the lack of 3D data, the plane stress case was used to solve the inverse problem, and as previously discussed, this does not make it possible to describe exactly the biological medium deformation when compressed with the ultrasound probe, which is inherently a 3D problem. When compression-induced displacement fields deviate from those that would be obtained under plane stress conditions, errors inevitably occur, as clearly illustrated with the 3D simulations. The choice between plane stress and plane strain was made here, as the displacement fields measured experimentally were found to be closer to those obtained in the plane stress case, when performing a modeling of the experiments using COMSOL Multiphysics. These observations, however, were made from a few experiments using only two different phantoms. Therefore, it will be of interest to also investigate the plane strain-based reconstruction method and to conduct a thorough comparison between the plane stress- and plane strain-based approaches, as well as to go deeper into the analysis of the 3D problem. Such a study is beyond the scope of this paper, but will be part of future work.

For tests with phantoms, a comparison of the results with those from a commercial ultrasound scanner (Aixplorer) was made. This comparison was performed to better appreciate the results obtained with the proposed method and to determine whether this method deserves to be further developed. The Aixplorer ultrasound scanner, which comprises a shear wave-based elastography approach (supersonic shear imaging) was used, as the only clinical system we have access to. Nevertheless, the wide use of this scanner

in clinical practice and studies makes the given comparison of interest. The Aixplorer provides values of the local shear wave speed or of the Young's modulus, the latter being, as explained earlier, computed as three times the shear modulus considering that the media examined are linear elastic, isotropic, and (quasi-) incompressible. Consequently, any Young's modulus ratio provided by this system is equal to the shear modulus ratio. Moreover, when examining biological tissues with shear wave elastography techniques, it is well known that there is a frequency dependence of the modulus measurements, linked to the viscoelastic properties of the medium. For purely elastic materials, the modulus value remains the same, whatever the frequency of the shear wave. The phantoms used in this study and manufactured by CIRS are made of Zerdine hydrogel, described as being elastic, as shown also with some specific measurements and analysis performed in different studies (Andoh et al. (2021); Oudry et al. (2014)). These different elements allow us to conduct a direct comparison of the ratios from the two techniques.

Contrary to shear wave techniques, which give access to modulus values (in kPa), our reconstruction method only provides maps of the relative shear modulus of the examined media. However, such maps enable computation of the stiffness ratio between regions, which is also a criterion of interest for diagnosis. Indeed, when modifications occur locally within tissues, an increase in stiffness at that location will directly result in a higher ratio, when compared with a reference region. Many studies have shown that using qualitative and quantitative parameters from shear wave elastography, among which the modulus ratio, can be helpful for distinguishing between tissues (Berg et al. (2012); Au et al. (2014); Brunel et al. (2015)). Among the

other parameters studied are the mean and maximum elastic moduli, both directly providing information on the mechanical properties of the selected tissue area. These three parameters have been widely investigated, notably for the assessment of breast lesions. Results revealed that the mean modulus, maximum modulus and modulus ratio are all significantly higher for malignancies than for benign lesions, the best performing parameter varying with the studies (Berg et al. (2012); Au et al. (2014); Kim et al. (2014); Olgun et al. (2014); Xiao et al. (2016)). Consequently, relative shear modulus mapping as described in this paper can also provide useful information for diagnosis.

The developments presented are very recent, and additional work will be necessary to fully assess this approach. Although illustrating simplified situations, this first evaluation of the method with simulated and phantom data remains an essential step, keeping in mind that this method is developed for diagnostic purposes. Therefore, many other tests including *in vivo* biological tissues will need to be conducted, which can potentially lead to method modifications.

The proposed method is based on the variational formulation of the equilibrium equations. This approach avoids computing the spatial derivatives of the stress components. Unlike some methods discussed in the introduction, it therefore allows us to get rid of displacement second-order derivatives, which is particularly interesting in ultrasound elastography, as the lateral displacement fields estimated are typically more affected by noise than the axial fields. Moreover, since no spatial derivative of the stress components, and consequently of the Lamé parameters, needs to be computed, this approach

also allows us to get rid of the medium local homogeneity assumption, which can help improve the results as this assumption is not adapted to the examination of heterogeneous media like biological tissues (Scott et al. (2020)). The developments described in this article could therefore benefit other elastography techniques that use the local homogeneity assumption.

Conclusions

In this paper, an inversion method to reconstruct the stiffness contrast in QSUE has been presented, along with preliminary results from simulations and phantom experiments. This method is able to recover the different regions within a medium, with shear modulus ratios that clearly reveal the stiff and soft inclusions. Moreover, a comparison with a shear wave elastography technique available in a clinical ultrasound scanner showed that the inclusion-to-background shear modulus ratios obtained with the proposed approach were closer to the expected values. Future work will focus on a more thorough assessment of this approach, including *in vivo* biological tissues.

Conflict of interest disclosure

The authors declare no conflicts of interest.

Acknowledgments

The authors thank H. Ammari for fruitful discussions. The quasi-static ultrasound elastography data were acquired with equipment provided by PILOT (INSA-Lyon, France), and the images and modulus ratios from the

shear wave elastography technique were obtained using an Aixplorer ultrasound scanner from the Centre Léon Bérard (Lyon, France). Finally, part of this work was supported by the LABEX MILYON (ANR-10-LABX-0070) of Université de Lyon, within the program "Investissements d'Avenir" (ANR-11-IDEX-0007) operated by the French National Research Agency (ANR).

Data availability statement

Because of valorization strategies under study, the source code cannot currently be made available. The raw phantom data can be accessed at: `https://www.creatis.insa-lyon.fr/~brusseau/Elastography_UMB2022`

References

Ammari H, Bretin E, Millien P, Seppecher L. A direct linear inversion for discontinuous elastic parameters recovery from internal displacement information only. Numerische Mathematik, 2021;147:189–226.

Ammari H, Waters A, Zhang H. Stability analysis for magnetic resonance elastography. Journal of Mathematical Analysis and Applications, 2015;430:919–931.

Andoh F, Yue J, Julea F, Tardieu M, Noûs C, Pagé G, Garteiser P, Van Beers B, Maitre X, Pellot-Barakat C. Multifrequency magnetic resonance elastography for elasticity quantitation and optimal tissue discrimination: A two-platform liver fibrosis mimicking phantom study. NMR in Biomedicine, 2021;34:e4543.

Au FWF, Ghai S, Moshonov H, Kahn H, Brennan C, Dua H, Crystal P. Diagnostic performance of quantitative shear wave elastography in the evaluation of solid breast masses: determination of the most discriminatory parameter. American Journal of Roentgenology, 2014;203:W328–W336.

Baldewsing RA, Mastik F, Schaar JA, Serruys PW, van der Steen AF. Young's modulus reconstruction of vulnerable atherosclerotic plaque components using deformable curves. Ultrasound in Medicine & Biology, 2006;32:201–210.

Baldewsing RA, Schaar JA, Mastik F, Oomens CWJ, van der Steen AFW. Assessment of vulnerable plaque composition by matching the deforma-

tion of a parametric plaque model to measured plaque deformation. IEEE Transactions on Medical Imaging, 2005;24:514–528.

Bamber J, Cosgrove D, Dietrich CF, Fromageau J, Bojunga J, Calliada F, Cantisani V, Correas JM, D'Onofrio M, Drakonaki EE, Fink M, Friedrich-Rust M, Gilja OH, Havre RF, Jenssen C, Klauser AS, Ohlinger R, Saftoiu A, Schaefer F, Sporea I, Piscaglia F. EFSUMB guidelines and recommendations on the clinical use of ultrasound elastography. Part 1: basic principles and technology. Ultraschall in Der Medizin, 2013;34:169–184.

Barbone PE, Oberai AA. Elastic modulus imaging: some exact solutions of the compressible elastography inverse problem. Physics in Medicine and Biology, 2007;52:1577–1593.

Bercoff J, Tanter M, Fink M. Supersonic shear imaging: a new technique for soft tissue elasticity mapping. IEEE Transactions on Ultrasonics, Ferroelectrics and Frequency Control, 2004;51:396–409.

Berg WA, Cosgrove DO, Doré CJ, Schäfer FKW, Svensson WE, Hooley RJ, Ohlinger R, Mendelson EB, Balu-Maestro C, Locatelli M, Tourasse C, Cavanaugh BC, Juhan V, Stavros AT, Tardivon A, Gay J, Henry JP, Cohen-Bacrie C. Shear-wave elastography improves the specificity of breast US: the BE1 multinational study of 939 masses. Radiology, 2012;262:435–449.

Brunel T, Guibal A, Boularan C, Ducerf C, Mabrut JY, Bancel B, Boussel L, Rode A. Focal nodular hyperplasia and hepatocellular adenoma: The value

of shear wave elastography for differential diagnosis. European Journal of Radiology, 2015;84:2059–2064.

Brusseau E, Detti V, Coulon A, Maissiat E, Boublay N, Berthezène Y, Fromageau J, Bush N, Bamber J. In vivo response to compression of 35 breast lesions observed with a two-dimensional locally regularized strain estimation method. Ultrasound in Medicine & Biology, 2014;40:300–312.

Brusseau E, Petrusca L, Bretin E, Millien P, Seppecher L. Reconstructing the shear modulus contrast of linear elastic and isotropic media in quasi-static ultrasound elastography. In proc. of the 43rd Annual International Conference of the IEEE Engineering in Medicine and Biology Society (EMBC), 2021:3177–3180.

Chang JM, Won JK, Lee KB, Park IA, Yi A, Moon WK. Comparison of Shear-Wave and Strain Ultrasound Elastography in the Differentiation of Benign and Malignant Breast Lesions. American Journal of Roentgenology, 2013;201:W347–W356.

Cho N, Moon WK, Kim HY, Chang JM, Park SH, Lyou CY. Sonoelastographic strain index for differentiation of benign and malignant nonpalpable breast masses. Journal of Ultrasound in Medicine, 2010;29:1–7.

Cosgrove D, Piscaglia F, Bamber J, Bojunga J, Correas JM, Gilja O, Klauser A, Sporea I, Calliada F, Cantisani V, D'Onofrio M, Drakonaki E, Fink M, Friedrich-Rust M, Fromageau J, Havre R, Jenssen C, Ohlinger R, Săftoiu A, Schaefer F, Dietrich C. EFSUMB guidelines and recommendations on the clinical use of ultrasound elastography. Part 2: clinical applications.

Ultraschall in der Medizin - European Journal of Ultrasound, 2013;34:238–253.

Doyley MM. Model-based elastography: a survey of approaches to the inverse elasticity problem. Physics in Medicine and Biology, 2012;57:R35–R73.

Doyley MM, Meaney PM, Bamber JC. Evaluation of an iterative reconstruction method for quantitative elastography. Physics in Medicine and Biology, 2000;45:1521–1540.

Gong X, Xu Q, Xu Z, Xiong P, Yan W, Chen Y. Real-time elastography for the differentiation of benign and malignant breast lesions: a meta-analysis. Breast Cancer Research and Treatment, 2011;130:11–18.

Grant M, Boyd S. Graph implementations for nonsmooth convex programs. In: Blondel V, Boyd S, Kimura H (Eds.), Recent Advances in Learning and Control. Lecture Notes in Control and Information Sciences. Springer-Verlag Limited, 2008. pp. 95–110.

Grant M, Boyd S. CVX: Matlab software for disciplined convex programming, version 2.1. http://cvxr.com/cvx, 2014.

Hoerig C, Ghaboussi J, Insana MF. An information-based machine learning approach to elasticity imaging. Biomechanics and Modeling in Mechanobiology, 2017;16:805–822.

Hoerig C, Ghaboussi J, Insana MF. Data-driven elasticity imaging using cartesian neural network constitutive models and the autoprogressive method. IEEE Transactions on Medical Imaging, 2019;38:1150–1160.

Itoh A, Ueno E, Tohno E, Kamma H, Takahashi H, Shiina T, Yamakawa M, Matsumura T. Breast disease: clinical application of US elastography for diagnosis. Radiology, 2006;239:341–350.

Karimi H, Fenster A, Samani A. A novel fast full inversion based breast ultrasound elastography technique. Physics in Medicine and Biology, 2013;58:2219–2233.

Kim HJ, Kim SM, Kim B, La Yun B, Jang M, Ko Y, Lee SH, Jeong H, Chang JM, Cho N. Comparison of strain and shear wave elastography for qualitative and quantitative assessment of breast masses in the same population. Scientific Reports, 2018;8:6197.

Kim S, Choi S, Choi Y, Kook SH, Park H, Chung E. Diagnostic performance of shear wave elastography of the breast according to scanning orientation. Journal of Ultrasound in Medicine, 2014;33:1797–1804.

Krouskop TA, Wheeler TM, Kallel F, Garra BS, Hall T. Elastic moduli of breast and prostate tissues under compression. Ultrasonic Imaging, 1998;20:260–274.

Lyshchik A, Higashi T, Asato R, Tanaka S, Ito J, Mai JJ, Pellot-Barakat C, Insana MF, Brill AB, Saga T, Hiraoka M, Togashi K. Thyroid gland tumor diagnosis at US elastography. Radiology, 2005;237:202–211.

Mariappan YK, Glaser KJ, Ehman RL. Magnetic resonance elastography: a review. Clinical Anatomy, 2010;23:497–511.

Mazza E, Nava A, Hahnloser D, Jochum W, Bajka M. The mechanical response of human liver and its relation to histology: an in vivo study. Medical Image Analysis, 2007;11:663–672.

Nayak R, Huntzicker S, Ohayon J, Carson N, Dogra V, Schifitto G, Doyley M. Principal strain vascular elastography: simulation and preliminary clinical evaluation. Ultrasound in Medicine and Biology, 2017;43:682–699.

Nitta N, Shiina T. A method of tissue elasticity estimation based on three-dimensional displacement vector. Japanese Journal of Applied Physics, 2000;39:3225–3229.

Olgun D, Korkmazer B, Kılıç F, Dikici A, Velidedeoğlu M, Aydoğan F, Kantarcı F, Yılmaz M. Use of shear wave elastography to differentiate benign and malignant breast lesions. Diagnostic and Interventional Radiology, 2014;20:239–244.

Ophir J, Céspedes I, Ponnekanti H, Yazdi Y, Li X. Elastography: a quantitative method for imaging the elasticity of biological tissues. Ultrasonic Imaging, 1991;13:111–134.

Oudry J, Lynch T, Vappou J, Sandrin L, Miette V. Comparison of four different techniques to evaluate the elastic properties of phantom in elastography: is there a gold standard? Physics in Medicine and Biology, 2014;59:5775–5793.

Parker KJ, Doyley MM, Rubens DJ. Imaging the elastic properties of tissue: the 20 year perspective. Physics in Medicine and Biology, 2011;56:R1–R29.

Poul S, Parker K. Fat and fibrosis as confounding cofactors in viscoelastic measurements of the liver. Physics in Medicine and Biology, 2021;66:045024.

Scott J, Arani A, Manduca A, McGee K, Trzasko J, Huston III J, Ehman R, Murphy M. Artificial neural networks for magnetic resonance elastography stiffness estimation in inhomogeneous materials. Medical Image Analysis, 2020;63:101710.

Seidl DT, Oberai AA, Barbone PE. The coupled adjoint-state equation in forward and inverse linear elasticity: Incompressible plane stress. Computer Methods in Applied Mechanics and Engineering, 2019;357:112588.

Seo M, Ahn HS, Park SH, Lee JB, Choi BI, Sohn YM, Shin SY. Comparison and Combination of Strain and Shear Wave Elastography of Breast Masses for Differentiation of Benign and Malignant Lesions by Quantitative Assessment: Preliminary Study. Journal of Ultrasound in Medicine, 2018;37:99–109.

Sumi C, Suzuki A, Nakayama K. Estimation of shear modulus distribution in soft tissue from strain distribution. IEEE Transactions on Biomedical Engineering, 1995;42:193–202.

Tanter M, Bercoff J, Athanasiou A, Deffieux T, Gennisson J, Montaldo G, Muller M, Tardivon A, Fink M. Quantitative assessment of breast lesion viscoelasticity: Initial clinical results using supersonic shear imaging. Ultrasound in Medicine & Biology, 2008;34:1373–1386.

Thittai A, Galaz B, Ophir J. On the advantages of imaging the axial-shear strain component of the total shear strain in breast tumors. Ultrasound in Medicine and Biology, 2012;38:2031–2037.

Varghese T. Quasi-static ultrasound elastography. Ultrasound Clinics, 2009;4:323–338.

Waage JER, Havre RF, Ødegaard S, Leh S, Eide GE, Baatrup G. Endorectal elastography in the evaluation of rectal tumours. Colorectal Disease, 2011;13:1130–1137.

Wang S, Larin KV. Optical coherence elastography for tissue characterization: a review. Journal of Biophotonics, 2015;8:279–302.

Widlak T, Scherzer O. Stability in the linearized problem of quantitative elastography. Inverse Problems, 2015;31:035005.

Xiao Y, Yu Y, Niu L, Qian M, Deng Z, Qiu W, Zheng H. Quantitative evaluation of peripheral tissue elasticity for ultrasound-detected breast lesions. Clinical Radiology, 2016;71:896–904.

Youk JH, Son EJ, Gweon HM, Kim H, Park YJ, Kim JA. Comparison of Strain and Shear Wave Elastography for the Differentiation of Benign From Malignant Breast Lesions, Combined With B-mode Ultrasonography: Qualitative and Quantitative Assessments. Ultrasound in Medicine & Biology, 2014;40:2336–2344.

Figure Captions

Figure 1: Honeycomb space discretization, with h the edge size (black), and adapted triangular sub-mesh (dashed blue).

Figure 2: Graph of the test function φ_i.

Figure 3: Example of a displacement field before regularization, obtained from a phantom experiment (CIRS model 049, Type III inclusion). (a) axial displacement, u_y (in mm), and (b) lateral displacement, u_x (in mm). In (a), axes are in millimeters.

Figure 4: Derivatives of the displacement components before regularization, obtained from the fields displayed in Figure 3. (a) axial strain ($\partial_y u_y$), (b) lateral-shear strain ($\partial_y u_x$), (c) axial-shear strain ($\partial_x u_y$), and (d) lateral strain ($\partial_x u_x$).

Figure 5: Displacement components after regularization and their derivatives for the CIRS model 049, Type III inclusion. (a) axial displacement, w_y (in mm), (b) lateral displacement, w_x (in mm), (c) axial strain ($\partial_y w_y$), (d) lateral-shear strain ($\partial_y w_x$), (e) axial-shear strain ($\partial_x w_y$), and (f) lateral strain ($\partial_x w_x$). In (a), axes are in mm.

Figure 6: 3D simulations - Illustration of the configuration of a medium compressed with the ultrasound transducer. The dashed lines indicate the positions of the axial and lateral displacement images selected for relative shear modulus reconstruction.

Figure 7: Relative shear modulus maps obtained with the plane stress simulations, for media characterized by inclusion-to-background shear mod-

ulus ratios of (a) 4/9 (case #1), (b) 16/9 (case #2), and (c) 27/9 (case #3). Axes are in mm.

Figure 8: Relative shear modulus maps obtained with the 3D simulations, for media characterized by inclusion-to-background shear modulus ratios of (a) 4/9 (case #4), (b) 16/9 (case #5), and (c) 27/9 (case #6). Axes are in mm.

Figure 9: Experimental results obtained with the CIRS phantoms. (a) Model 049, Type II inclusion (case #7), (b) model 049, Type III inclusion (case #8), (c) model 059, single inclusion (case #9), and (d) model 059, two inclusions (case #10). Axes are in mm.

Figure 10: Young's modulus images (in kPa) obtained with the Aixplorer ultrasound scanner. (a) Model 049, Type II inclusion (case #7), (b) model 049, Type III inclusion (case #8), (c) model 059, single inclusion (case #9), and (d) model 059, two inclusions (case #10).

Figure 11: Illustration of region selection for modulus ratio computation with the scanned area containing a single inclusion in the breast elastography phantom (case #9). Regions selected in the map reconstructed with (a) our method, and (b) and (c) the Aixplorer.

Tables

Table 1: Inclusion-to-background shear modulus ratios: results from plane stress and 3D simulations.

	Case #	Target ratio	R_1	R_2	R_{tb}
Plane stress simulations	1	0.44	0.43	0.43	0.44
	2	1.78	1.81	1.81	1.81
	3	3.00	3.11	3.11	3.08
3D simulations	4	0.44	0.55	0.58	0.60
	5	1.78	1.60	1.69	1.68
	6	3.00	2.62	2.79	2.74

Table 2: Inclusion-to-background shear modulus ratios: experimental results and comparison with the Aixplorer ultrasound scanner.

	Case #	Target ratio	Our method			Aixplorer	
			R_1	R_2	R_{tb}	R_1	R_2
CIRS 049	7	0.49	0.50	0.52	0.52	0.49	0.50
CIRS 049	8	1.77	1.73	1.77	1.76	1.38	1.59
CIRS 059	9	3.33	2.51	2.69	2.60	2.11	2.19
CIRS 059 (top)	10	3.33	2.48	2.70	2.35	2.01	2.33
CIRS 059 (bottom)	10	3.33	2.46	2.68	2.49	2.30	2.34

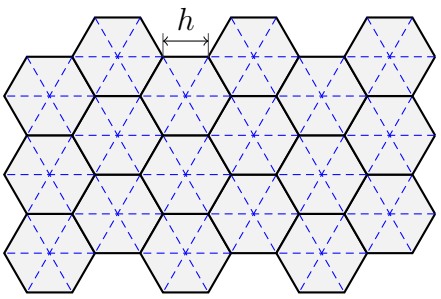

Figure 1: Honeycomb space discretization, with h the edge size (black), and adapted triangular sub-mesh (dashed blue).

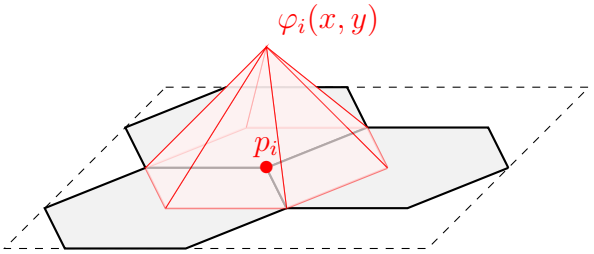

Figure 2: Graph of the test function φ_i.

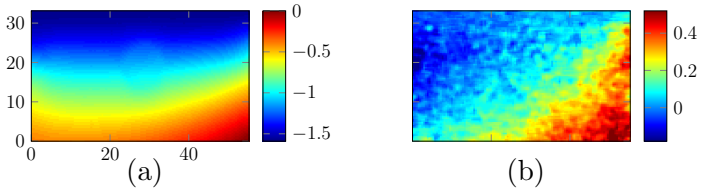

Figure 3: Example of a displacement field before regularization, obtained from a phantom experiment (CIRS model 049, Type III inclusion). (a) axial displacement, u_y (in mm), and (b) lateral displacement, u_x (in mm). In (a), axes are in millimeters.

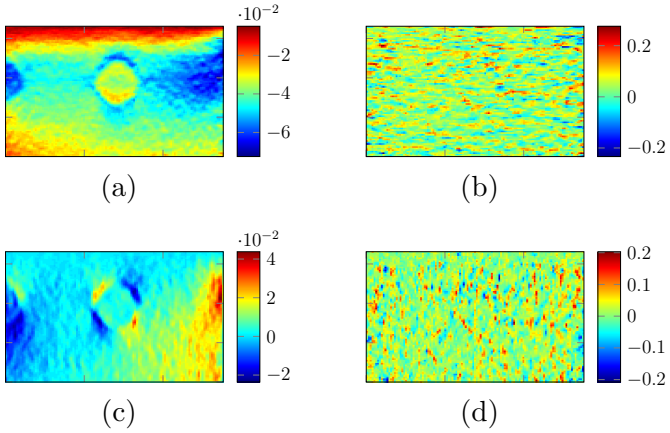

Figure 4: Derivatives of the displacement components before regularization, obtained from the fields displayed in Figure 3. (a) axial strain ($\partial_y u_y$), (b) lateral-shear strain ($\partial_y u_x$), (c) axial-shear strain ($\partial_x u_y$), and (d) lateral strain ($\partial_x u_x$).

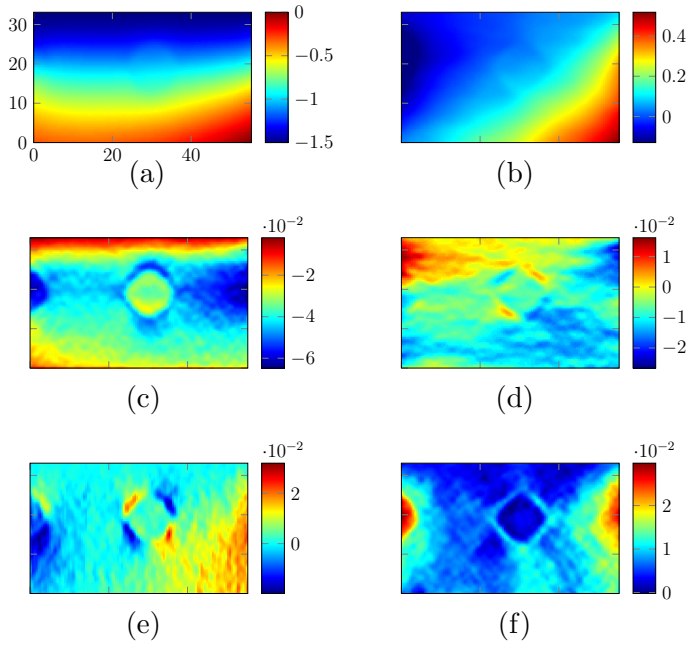

Figure 5: Displacement components after regularization and their derivatives for the CIRS model 049, Type III inclusion. (a) axial displacement, w_y (in mm), (b) lateral displacement, w_x (in mm), (c) axial strain ($\partial_y w_y$), (d) lateral-shear strain ($\partial_y w_x$), (e) axial-shear strain ($\partial_x w_y$), and (f) lateral strain ($\partial_x w_x$). In (a), axes are in mm.

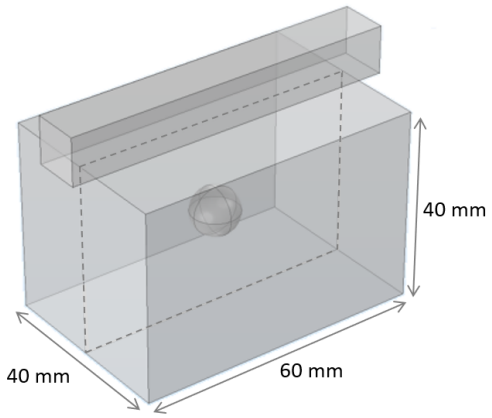

Figure 6: 3D simulations - Illustration of the configuration of a medium compressed with the ultrasound transducer. The dashed lines indicate the positions of the axial and lateral displacement images selected for relative shear modulus reconstruction.

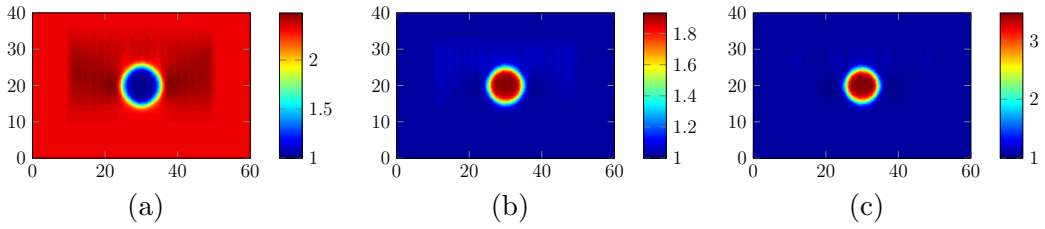

Figure 7: Relative shear modulus maps obtained with the plane stress simulations, for media characterized by inclusion-to-background shear modulus ratios of (a) 4/9 (case #1), (b) 16/9 (case #2), and (c) 27/9 (case #3). Axes are in mm.

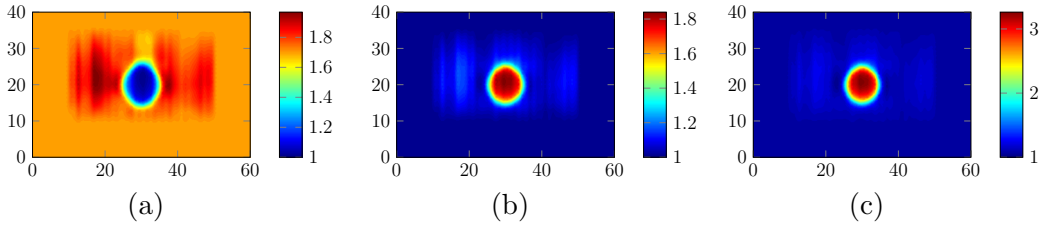

Figure 8: Relative shear modulus maps obtained with the 3D simulations, for media characterized by inclusion-to-background shear modulus ratios of (a) 4/9 (case #4), (b) 16/9 (case #5), and (c) 27/9 (case #6). Axes are in mm.

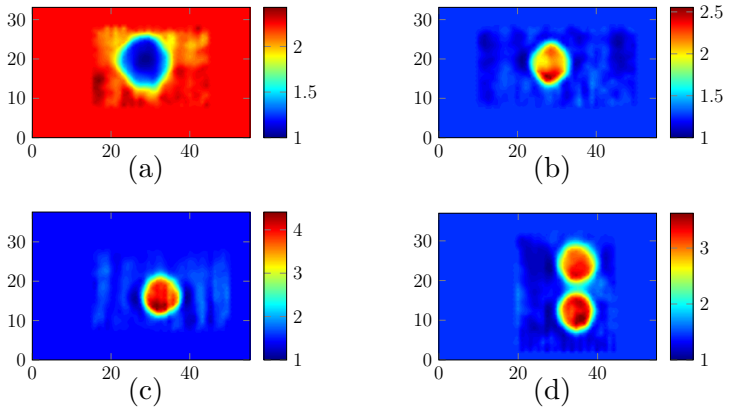

Figure 9: Experimental results obtained with the CIRS phantoms. (a) Model 049, Type II inclusion (case #7), (b) model 049, Type III inclusion (case #8), (c) model 059, single inclusion (case #9), and (d) model 059, two inclusions (case #10). Axes are in mm.

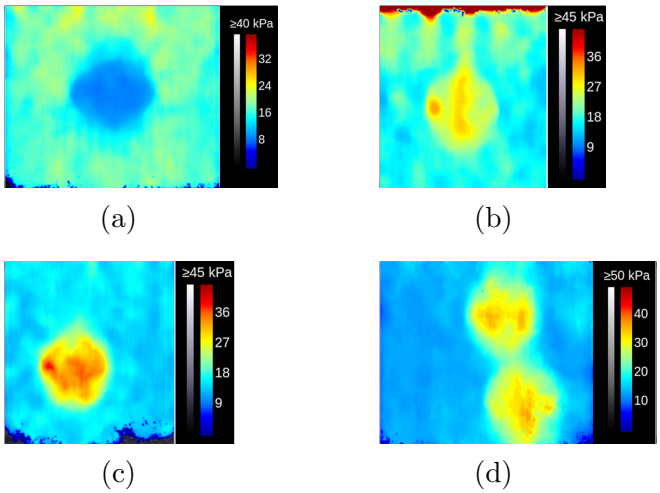

Figure 10: Young's modulus images (in kPa) obtained with the Aixplorer ultrasound scanner. (a) Model 049, Type II inclusion (case #7), (b) model 049, Type III inclusion (case #8), (c) model 059, single inclusion (case #9), and (d) model 059, two inclusions (case #10).

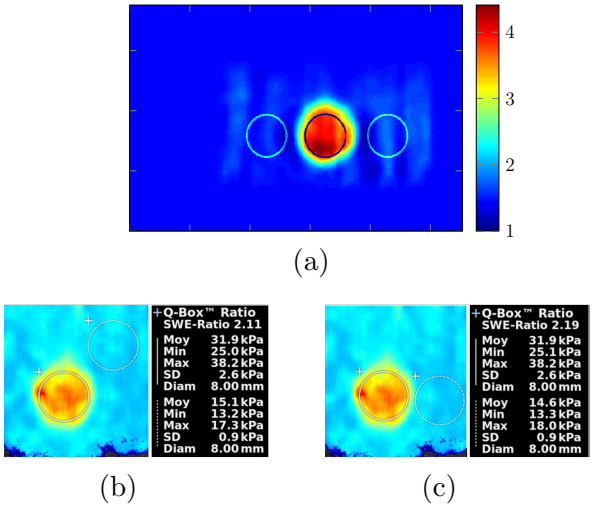

Figure 11: Illustration of region selection for modulus ratio computation with the scanned area containing a single inclusion in the breast elastography phantom (case #9). Regions selected in the map reconstructed with (a) our method, and (b) and (c) the Aixplorer.